Journal of Catalysis 418 (2023) 51–63

Contents lists available at ScienceDirect

Journal of Catalysis

journal homepage: www.elsevier.com/locate/jcat

Facile fabrication of heterostructured $BiPS_4$-Bi_2S_3-$BiVO_4$ photoanode for enhanced stability and photoelectrochemical water splitting performance

Maged N. Shaddad [a,1], Prabhakarn Arunachalam [a,1,*], Mahmoud Hezam [b,c], Norah M BinSaeedan [a], Sixto Gimenez [d], Juan Bisquert [d], Abdullah M. Al-Mayouf [a,e,*]

[a] Electrochemical Sciences Research Chair, Department of Chemistry, Science College, King Saud University, Riyadh, Saudi Arabia
[b] King Abdullah Institute for Nanotechnology, King Saud University, Riyadh, Saudi Arabia
[c] Department of Physics, College of Science, Imam Mohammad Ibn Saud Islamic University (IMSIU), Riyadh 13318, Saudi Arabia
[d] Institute of Advanced Materials (INAM), Unversitat Jaume I, 12006 Castelló de la Plana, Spain
[e] K.A. CARE Energy Research and Innovation Center at Riyadh, Saudi Arabia

ARTICLE INFO

Article history:
Received 22 May 2022
Revised 14 December 2022
Accepted 27 December 2022
Available online 30 December 2022

Keywords:
Bismuth vanadate
Photo-electro-transformation
Bismuth Sulfide
Metal Phosphorous Trichalcogenides
Electrolyte tuning

ABSTRACT

Bismuth vanadate ($BiVO_4$) is the most favorable electrode candidate for photoelectrochemical (PEC) water-splitting reactions. The poor charge separation and sluggish water oxidation dynamics are, however, the major setbacks of $BiVO_4$ photoanodes. To address these issues, we demonstrate that bismuth thiophosphate ($BiPS_4$)-Bi_2S_3 hybrid nanostructure was photoelectrochemically transformed on $BiVO_4$ electrodes ($BiPS_4$-Bi_2S_3-Bi_2O_3) when treated in Na_2S/PBS electrolyte, and a notable photocurrent of 3.5 mA/cm^2 at 0.65 V_{RHE} was obtained showing promising stability. X-ray photoelectron spectroscopy (XPS) and scanning electron microscopy (SEM) examination evidenced the effective makeover of $BiVO_4$ into the $BiPS_4$-Bi_2S_3/$BiVO_4$ nanostructured matrix. A negatively shifted onset potential and enriched durability are achieved for heterostructured $BiPS_4$-Bi_2S_3/$BiVO_4$ photoanodes due to decreased surface recombination. Interestingly, the Bode phase analysis evidenced the faster hole consumption in the water oxidation process in the $BiPS_4$-Bi_2S_3/$BiVO_4$ electrode compared to pristine $BiVO_4$. This methodology can be engaged to design different complex nanostructured materials with tunable optical and electrical features for photoelectrocatalysis, electrical energy storage, and solar cell uses.

1. Introduction

Solar radiation is a virtually inexhaustible and clean energy resource. Solar H_2 generation is accepted as a highly favorable technology to exploit solar energy and produce sustainable chemical fuels, tackling climate change stemming from the combustion of fossil fuels [1]. However, the efficient future use of solar energy to satisfy global energy demand is still dependent on developing efficient devices for energy conversion, storage, and distribution. The transformation of solar energy into hydrogen fuel, a clean and storable fuel, is a promising and active technological research field. Solar-driven water photo electro-catalysis (PEC) using semiconductor materials to produce hydrogen fuel has been a leading approach [2]. It is compulsory to develop highly efficient electrode materials that absorb a major portion of the solar irradiance, with suitable conduction band (CB) edge levels, chemical inertness, and cost-effectiveness.

Up to now, various *n*-type semiconductor photoanodes have been advanced for solar hydrogen production, such as TiO_2 [3], Fe_2O_3 [4], WO_3 [5], and $BiVO_4$ [6]. In particular, *n*-type $BiVO_4$ is one of the most attractive photoanodes owing to its favorable optoelectronic and photoelectrochemical properties such as relatively narrow bandgap, natural inertness, and appropriate energy level positions for water oxidation, and cost-effective [7–8]. The maximum theoretical photocurrent for $BiVO_4$ electrodes, with its narrow bandgap of ~2.4 eV, is ~7.5 mA/cm^2 at 1.23 V_{RHE}. Also, $BiVO_4$ can obtain a theoretic Solar-To-Hydrogen efficiency of 9.2 % [9]. Though, the most severe issue associated with $BiVO_4$ catalysts is the recombination of charge carriers, limiting its photocat-

* Corresponding authors.
E-mail addresses: parunachalam@ksu.edu.sa, amayouf@ksu.edu.sa (A.M. Al-Mayouf).
[1] These authors contributed equally to this work.

https://doi.org/10.1016/j.jcat.2022.12.032
0021-9517/

alytic efficiency as it results in a relatively short carrier diffusion length (ca. 70 nm) [10–11]. In literature, the identified photocurrent response for the bare $BiVO_4$ electrodes is thus generally < 1 mA/cm^2 at 1.23 V_{RHE} [12]. To overcome these concerns, different approaches such as facet modifications [13], morphology control [14], impurity doping [15–17], oxygen evolution catalyst deposition [18–19], and construction of p-n or *n-n* heterostructures [20] have been developed to upsurge the photon absorption and carrier transport of $BiVO_4$. More importantly, developing type II heterostructures is a favorable route to boost the charge transfer efficiency by creating an effective charge cascade and improving the visible-light absorption with other materials. For instance, Ying et al. fabricated $BiVO_4/Bi_2O_3$ heterostructured photoanodes by solvothermal synthesis and examined the photodegradation of methyl orange under illumination [21]. Further, Chae group reported $WO_3/BiVO_4$ photoanodes to boost the efficiency of solar-driven water splitting by improving the charge transfer and light absorption ability [22]. Regmi et al. demonstrated that hydrothermally fabricated $BiOBr/BiVO_4$ photoanodes improve malachite green degradation efficiency under visible-light excitation [23]. More recently, Ta et al. demonstrated the 3D-structured WO_3/Mo:$BiVO_4$ heterostructured photoanodes for PEC water oxidation reaction under acidic and neutral aqueous electrolytes. Moreover, we have developed $BiVO_4$/AgPi [24], $BiVO_4$/Ni-Fe Prussian blue [25], $BiVO_4$/Ag-Ni-OH-Pi [26], and $SnO_2/BiVO_4/NiWO_4$ [27] heterojunction-based photoanodes, showing enhanced performance compared to bare $BiVO_4$, owed to the well-separated and long-life photoinduced charge carriers for redox reaction offered by the developed heterojunctions. Since the oxygen Evolution Reaction (OER) is the most critical and so determining step toward the generation of solar Hydrogen from water splitting, the deposition of suitable co-catalytic materials in photocatalytic OER is mandatory. In this context, several research works combine OER catalysts over $BiVO_4$ photoanodes to improve charge transfer kinetics. For instance, CoPi, CoO_x, and $NiFeO_x$ electrocatalysts are decorated onto $BiVO_4$ electrodes [28–31], decreasing the surface recombination at the interface and/or enhancing OER kinetics.

On the other hand, Bi_2S_3 with a low bandgap of 1.4 eV has an appropriate energy level position that matches well with $BiVO_4$ for efficient charge separation and can be coupled with $BiVO_4$ to develop heterostructured photoanodes [32]. Indeed, there are some seminal studies of $BiVO_4/Bi_2S_3$ heterostructured electrodes for PEC water splitting. Notably, Liu et al. demonstrated $BiVO_4/Bi_2S_3$ nanowires heterostructured photoanode via a hydrothermal route and achieved a photocurrent response of 0.51 mA/cm^2 [33]. Zhuo et al. showed walnut-like $BiVO_4/Bi_2S_3$ heterostructured photoanodes with improved photocatalytic performance [34]. Particularly, Chen et al. designed $BiVO_4/Bi_2S_3$ heterostructured electrodes over conducting films and reached a remarkable photocurrent response of 1.43 mA/cm^2 under illumination [35]. On another hand, $BiPS_4$ is a solar absorber with suitable energy level positions that also match $BiVO_4$ for efficient electron-hole pairs separation [36]. These studies inspired us to explore $BiVO_4/Bi_2S_3$-$BiPS_4$ triple-layer heterostructured photoanodes as promising electrodes for PEC water splitting.

Herein, we describe a controlled electrochemical ion exchange strategy for producing a thin and homogenous $Bi_2S_3/BiPS_4$ film transformed over the surface of $BiVO_4$ electrodes, and its PEC features for water oxidation. The synthesized $BiVO_4/Bi_2S_3$-$BiPS_4$ heterostructured electrodes demonstrated a photocurrent response of $\sim$ 3.7 mA cm^{-2} at 1.23 V_{RHE} showing almost 5-fold enhancement related to bare $BiVO_4$ electrodes. The development of heterostructured electrodes based on $BiVO_4$ and Bi_2S_3-$BiPS_4$ has stronger light absorption, enhanced carrier separation, and remarkable transport and surface features.

2. Materials and methods

2.1. Materials

Bismuth(III) nitrate [$Bi(NO_3)_3{\cdot}5H_2O$, ≥99.0 %], vanadyl acetylacetonate [$VO(acac)_2$, ≥98.0 %], Sodium sulfide (Na_2S, ≥99.0 %), sodium sulfite (Na_2SO_3, ≥99.0 %), sodium sulfate (Na_2SO_4, ≥99.0 %), Dimethylsulfoxide (DMSO, ≥ 99.9 %) and ethylene glycol (EG, ≥99 %) were received from Sigma Aldrich. A Millipore system was adapted to acquire high-quality water to prepare the electrolyte solutions.

2.2. Fabrication of $BiVO_4$ photoanodes

$BiVO_4$ photoelectrodes were obtained via dual deposition process described by Choi et al [37]. An EG solution comprising 20 mM of $Bi(NO_3)_3{\cdot}5H_2O$ was acquired as the plating solution. The electrodeposition was executed by applying 0.04C/cm^2 at E = -1.8 V vs Ag/AgCl, followed by a relaxing time of 2 s. Subsequently, this electrochemical cycle was continual 8 times to give an entire charge of 0.40C/cm^2. Then, 60 µL of a DMSO solution involving 0.2 M $VO(acac)_2$ was kept over the as-deposited Bi electrode to completely protect their surface and was then subjected to a muffle furnace at 500 °C for 2 h in the air (rate = 2 °C/min) to convert Bi to $BiVO_4$. Left-over VO^{+2} ion was eliminated by drenching them in 1 M NaOH for 20 min and dried in air.

2.3. Fabrication of $BiVO_4/Bi_2S_3$ heterostructured photoanodes

The $BiVO_4/Bi_2S_3$ heterostructured photoanodes were fabricated by PEC transformation via an ion-exchange process in the aqueous medium comprising two sulfur species (Na_2S/Na_2SO_3) or (Na_2S/Na_2SO_4). The PEC transformation process was carried out in a classical PEC cell, under visible-light excitation (100 mW/cm^2) and cyclic voltammetry scans at 50 mV/s. $BiVO_4$ was electrodeposited over FTO glass (Hartford glass, 15 Ω/cm^2) and was employed as the working electrode, while Pt and Ag/AgCl were the counter and reference electrodes. During this PEC treatment, the Bi_2S_3 particles decorated over the $BiVO_4$ electrode surface. Lastly, the PEC ion-exchange process transformed yellow-colored $BiVO_4$ into black-colored $BiVO_4/Bi_2S_3$ heterostructured photoanodes. The synthetic method employed for the PEC transformation of $BiVO_4$ into $BiVO_4/Bi_2S_3$ heterostructured photoanodes is presented in Scheme S1.

2.4. Synthesis of $BiVO_4/Bi_2S_3/BiPS_4$ hybrid nanostructures

$BiPS_4$ was decorated over the $BiVO_4/Bi_2S_3$ heterostructured photoanodes via a subsequent PEC deposition process under visible-light excitation in a Na_2S/PBS electrolyte solution. After the ion-exchange process in the aqueous solution, both $BiPS_4$ and Bi_2S_3 particles decorated the surface of $BiVO_4$. The proposed reaction mechanisms are detailed below:

(1. In solution)

$$4S^{2-}_{(aq)} + [PO_4]^{3-}_{(aq)} + 8H^{+}_{(aq)} \rightleftarrows [PS_4]^{3-}_{(aq)} + 4H_2O \quad (1)$$

(2. Solid-liquid interface)

$$[PS_4]^{3-}_{(aq)} + Bi^{3+} \rightleftarrows BiPS_{4\,(s)} \quad (2)$$

2.5. Characterization

X-ray Diffraction (XRD) spectra were executed with Rigaku Miniflex-600 equipment. Surface analysis was executed using XPS (Specs SAGE 150), Where a morphological examination of

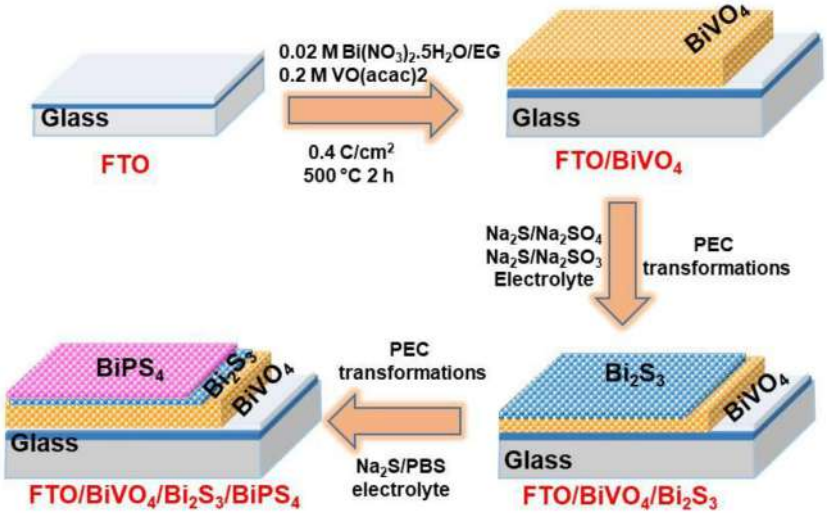

Scheme 1. Synthesis of Triple-layer heterostructured nanostructures. Schematic illustration of $BiVO_4/Bi_2S_3/BiPS_4$ heterostructured film on an FTO deposited via a developed PEC ion-exchange process.

the electrodes was carried out by Field Emission SEM with a JEOL JSM-7000F system.

2.6. Photoelectrochemical measurements

PEC features of the obtained films were examined by assessing their photocurrent density through a water-splitting reaction. The photocurrent response was evaluated through a potentiostat (Autolab, PGSTAT30). PEC examination of the electrodes was carried out through CV and LSV under-stimulated light conditions (100 mW/cm^2) in 0.1 M Na_2S/PBS (pH 10). Also, electrochemical impedance spectroscopy (EIS) (100 kHz-100 mHz) study was obtained through an electrochemical system in 0.1 M PBS solution at 0.65 V_{RHE} under illumination situvations.

3. Results and discussion

3.1. Materials characterization

Bismuth thiophosphate ($BiPS_4$) was decorated over $BiVO_4$ via ion-exchange reactions in an electrolyte comprising 0.1 M PBS/Na_2S solution. Particularly, Scheme S1 shows the sequential steps of the synthetic method for fabricating the $BiVO_4/Bi_2S_3/BiPS_4$ photoanodes. Notably, the adsorbed water over the electrode surface generates OH^- ions during the CV scans. Also, $BiVO_4/Bi_2S_3$ and bare $BiVO_4$ photoanodes were obtained using an electrodeposition process on FTO, as described in the experimental Methods.

The morphological characterization during the various stages of the synthetic process of the $BiVO_4/Bi_2S_3$-$BiPS_4$ composite photoanodes was carried out through FE-SEM. The optimal $BiVO_4$ photoanodes were initially transformed with Bi_2S_3 catalysts by ion-exchange reactions in 0.1 M Na_2SO_3. For comparison, Fig. 1a, b shows the FE-SEM photographs of $BiVO_4$ films; the anodes keep the smoother-edged dendrites with a large surface area. Fig. 1c displays the FE-SEM micrographs of the Bi_2S_3 nanoparticles through ion exchange reactions (10 cycles) on the $BiVO_4$ ($BiVO_4/Bi_2S_3$-1) photoanodes prepared in 0.1 M Na_2SO_4 + Na_2S electrolytes. The FE-SEM images of $BiVO_4/Bi_2S_3$ electrodes display direct evidence of Bi_2S_3 loading was homogenous and very thin on the $BiVO_4$ surface (Fig. 1d). Fabricated $BiVO_4/Bi_2S_3$ photoanodes were then transformed into $BiVO_4/Bi_2S_3$-$BiPS_4$ by PEC treatment (via 10 CV scans) in 0.1 M PBS (Fig. 1e). Finally, as seen in Fig. 1f, the FESEM photographs of $BiVO_4/Bi_2S_3$-$BiPS_4$ obviously disclose that the $BiVO_4$ surface became homogenously smoother after incorporating phosphate.

Fig. 2a illustrates the X-ray diffraction patterns for the bare $BiVO_4$ before and after incorporating Bi_2S_3 and $BiPS_4$ ($BiVO_4/Bi_2S_3$, $BiVO_4/Bi_2S_3/BiPS_4$) by the PEC ion-exchange process. There was substantial variation in the diffraction patterns of $BiVO_4/Bi_2S_3$ electrodes, validating the development of new phases in the modified $BiVO_4$ electrodes. For the bare $BiVO_4$ (black), sharp peaks assigned to the $BiVO_4$ electrode agreed with the JCPDS # 00–014-0688 and were denoted by the symbol (◆) [38–39]. After the introduction of Bi2S3, Fig. 2a (blue curve), the observed peaks agree with the Bi_2S_3 phase, corresponding to the JCPDS pattern (00–017–0320) of bare Bi_2S_3 [40–41], which were labeled as (Δ). Finally, the diffraction pattern of $BiVO_4/Bi_2S_3$-$BiPS_4$ hybrid nanostructures (red curve) validates the decoration of $BiPS_4$ over $BiVO_4/Bi_2S_3$, corresponding to the JCPDS file No. (1–071-0364), which were labeled as (♥) [42]. The diffraction patterns presented in Fig. 2a clearly display the presence of both Bi_2S_3 and $BiPS_4$ over the surface of $BiVO_4$. Further, Raman Spectroscopy was executed to assess the local structure of fabricated heterostructured photoanodes (Fig. 2b). The vibrational bands at ~ 210.9, 327, 369, and 830 cm^{-1} characteristics for $BiVO_4$ were observed for all the fabricated photoanodes consistent with the earlier works [43–45]. Also, the characteristic vibrational bands situated at 830 cm^{-1} correspond to the asymmetric and symmetric V–O stretching vibration mode, whereas the other Raman peaks at 210 cm^{-1}, 326 cm$^{-1,}$ and 371 cm^{-1} were allocated to the external vibration mode and asymmetric–symmetric bending vibrations of vanadates. However, in the decorated samples, the observed blue shifts in the major Raman bands were related to symmetric V–O stretching, reflecting asymmetry in the crystalline structure and evidently witnessed in $BiVO_4/Bi_2S_3$-$BiPS_4$ photoanodes. This electrode reveals the presence of the most intense Raman band owed to symmetric V–O stretching ca. 830 cm^{-1}, indicating a higher degree of disorder for average vanadate species [46]. On the other hand, the thin homogenous Bi_2S_3-$BiPS_4$ can explain the absence of Raman modes that are specific to the Bi_2S_3-$BiPS_4$ coating. Hence, we can conclude that the Bi_2S_3-$BiPS_4$ hybrid heterostructures were successfully prepared through the electrochemical ion exchange treatment process with intimate modification to the $BiVO_4$ surface.

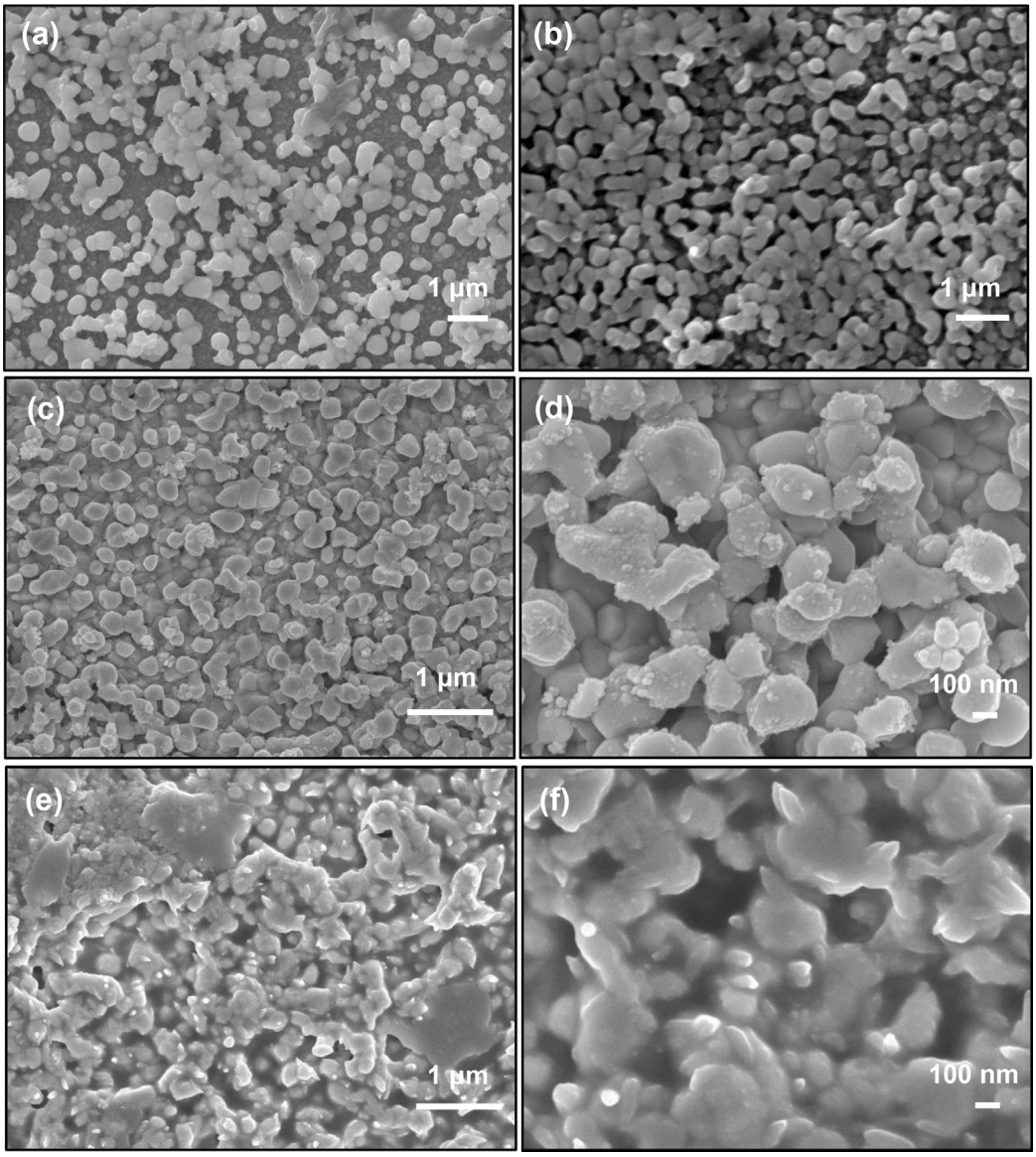

Fig. 1. FESEM micrographs of $BiVO_4$ photoanodes. FE-SEM photographs of the (a,b) $BiVO_4$ photoanodes obtained through electrochemical deposition process at different magnifications; (c,d) $BiVO_4/Bi_2S_3$ photoanodes obtained after 10 cycles in Na_2SO_3 electrolyte, and (e, f) $BiVO_4/BiPS_4$-Bi_2S_3 photoanodes obtained after 10 cycles under the treatment of Na_2S and PBS solution.

Fig. 3 illustrates UV–visible spectroscopy results of bare-$BiVO_4$ and $BiVO_4/Bi_2S_3$, and $BiVO_4/Bi_2S_3$-$BiPS_4$ samples acquired after 10 cycles under the treatment of Na_2S and PBS solution. Fig. 3a displays the absorption spectra of the three electrodes, while Fig. 3b shows their Tauc plots, where the bandgap for $BiVO_4$ was assessed to be 2.4 eV. It has to be mentioned here that the absorption spectra of both Bi_2S_3 and Bi_2S_3-$BiPS_4$ decorated electrodes showed long Urbach tails at the absorption onsets rendering it difficult to accurately estimate the bandgap edge from their Tauc plots. Fig. 3c shows a magnified image for both samples at the absorption onset region where the bandgap edge was assessed to be about 1.6 eV and 1.64 eV respectively for the Bi_2S_3 and Bi_2S_3-$BiPS_4$ decorated electrodes. Fig. 3d shows the correlation between F(R) and wavelength for fabricated electrodes. As shown in Fig. 3a, the light absorption capability of $BiVO_4$ is considerably improved after Bi_2S_3 was transformed. The combined deposition of Bi_2S_3 and $BiPS_4$ nanoparticles provide an additional synergetic enhancement of the optical density of the bare $BiVO_4$ electrodes in the visible-light region. More importantly, it illustrates that the decoration of the $BiPS_4$ and Bi_2S_3 particles over $BiVO_4$ can lead to the absorption of a higher fraction of the visible portion of the solar spectrum. In particular, when Bi_2S_3 was deposited, the extended absorption range is directly related to its narrow bandgap at $\sim$ 1.6 eV, where the visible spectrum between the absorption edge of $BiVO_4$ at $\sim$ 2.4 eV and that of Bi_2S_3 at $\sim$ 1.6 eV could now be absorbed. The large absorption coefficient of Bi_2S_3 is another possible reason behind the improved light harvesting. Notably, recent reports have proved that the Bi_2S_3 nanostructured particles have strong absorption over $BiVO_4$ [47], as demonstrated by the improved optical absorbance at λ > 500 nm in Fig. 3a. When $BiPS_4$, with its bandgap of $\sim$ 1.64 eV, was additionally introduced, the absorption onset in the absorption spectrum was clearly not affected due to the almost similar bandgap of Bi_2S_3 previously deposited. However, the optical density was remarkably enhanced (almost doubled over the whole absorption region). Therefore, the absorption spectrum of the $BiVO_4/Bi_2S_3$-$BiPS_4$ photoanodes was both stretched over a wider region and enhanced by a factor of $\sim$ 2.

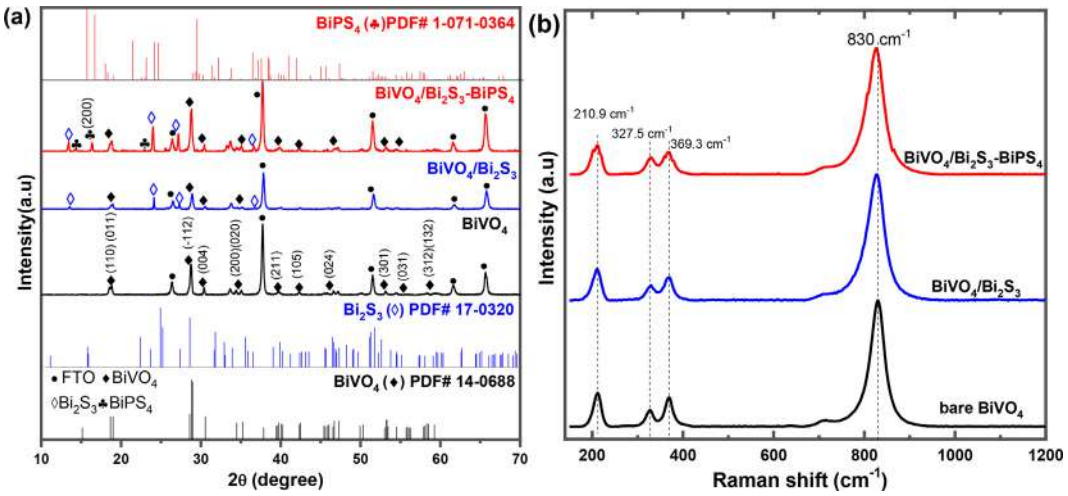

Fig. 2. Diffraction pattern of photoanodes. (a) Normalized X-ray diffraction pattern for $BiVO_4$, $BiVO_4/Bi_2S_3$ heterostructures, and $BiVO_4/Bi_2S_3$-$BiPS_4$ hybrid heterostructures prepared over FTO substrate through electrochemical ion exchange reactions. (b) Raman spectra of fabricated $BiVO_4$, $BiVO_4/Bi_2S_3$, and $BiVO_4/Bi_2S_3$-$BiPS_4$, obtained in the region of 150–1200 cm^{-1}.

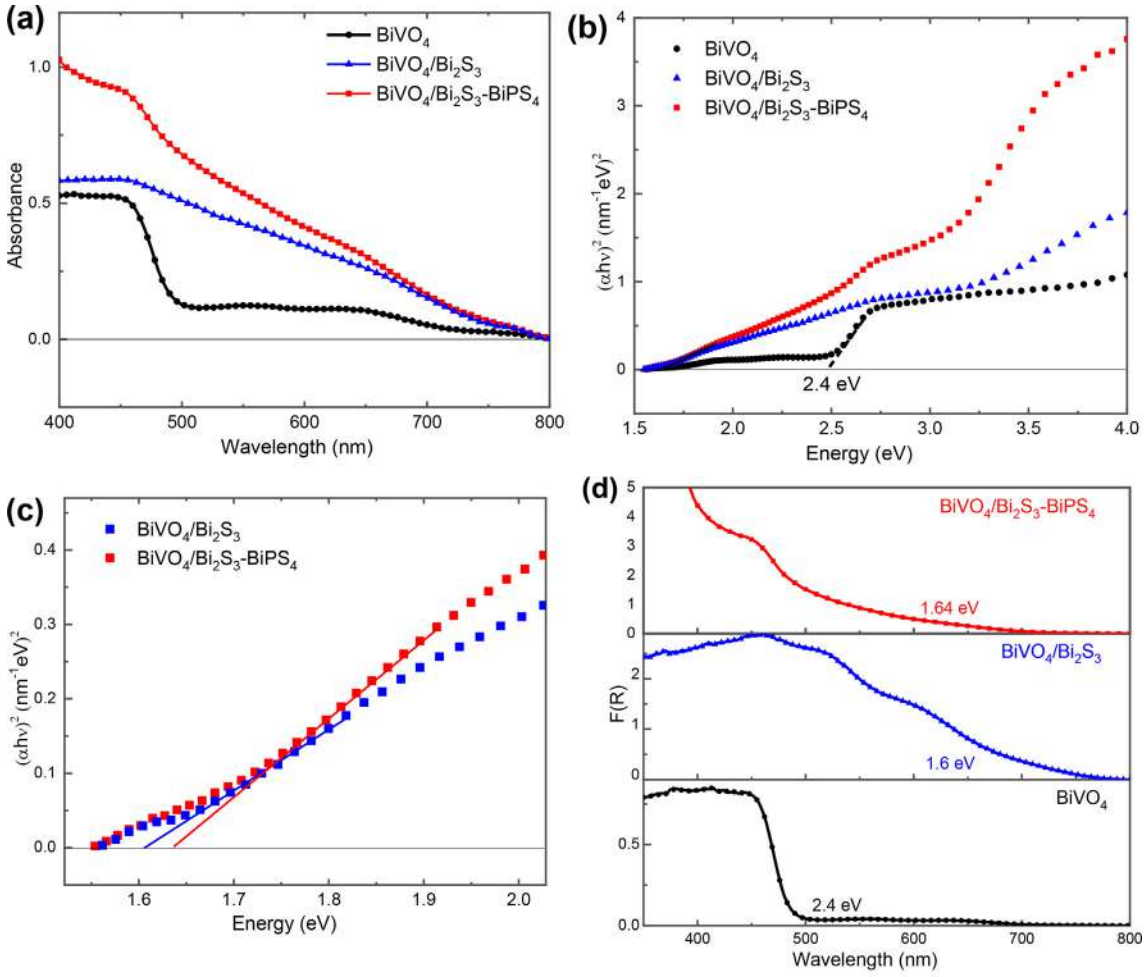

Fig. 3. Optical features of photoanodes. (a) UV–vis absorption spectra of $BiVO_4$, $BiVO_4/Bi_2S_3$, and $BiVO_4/Bi_2S_3$-$BiPS_4$ hybrid heterostructures prepared by means of electrochemical ion-exchange reactions, (b) the corresponding correlation between $(\alpha h\upsilon)^{1/2}$ and E (eV) for bare $BiVO_4$ and $BiVO_4/Bi_2S_3$, and $BiVO_4/Bi_2S_3$-$BiPS_4$ and their enlarged view (c) of electrodes, (d) the corresponding Kubelka-Munk function F(R) for bare $BiVO_4$ and $BiVO_4/Bi_2S_3$, and $BiVO_4/Bi_2S_3$-$BiPS_4$ with bandgaps of 2.4, 1.6, and 1.64 eV, respectively.

Moreover, the XPS study provides further insights into the interface between $BiVO_4$ and $BiPS_4$-Bi_2S_3. The obtained spectra are reported in Fig. 4. The full XPS survey spectra of Fig. 4a indicate that $BiVO_4/Bi_2S_3$-$BiPS_4$ contains Bi, V, O, P, and S. Also, the XPS

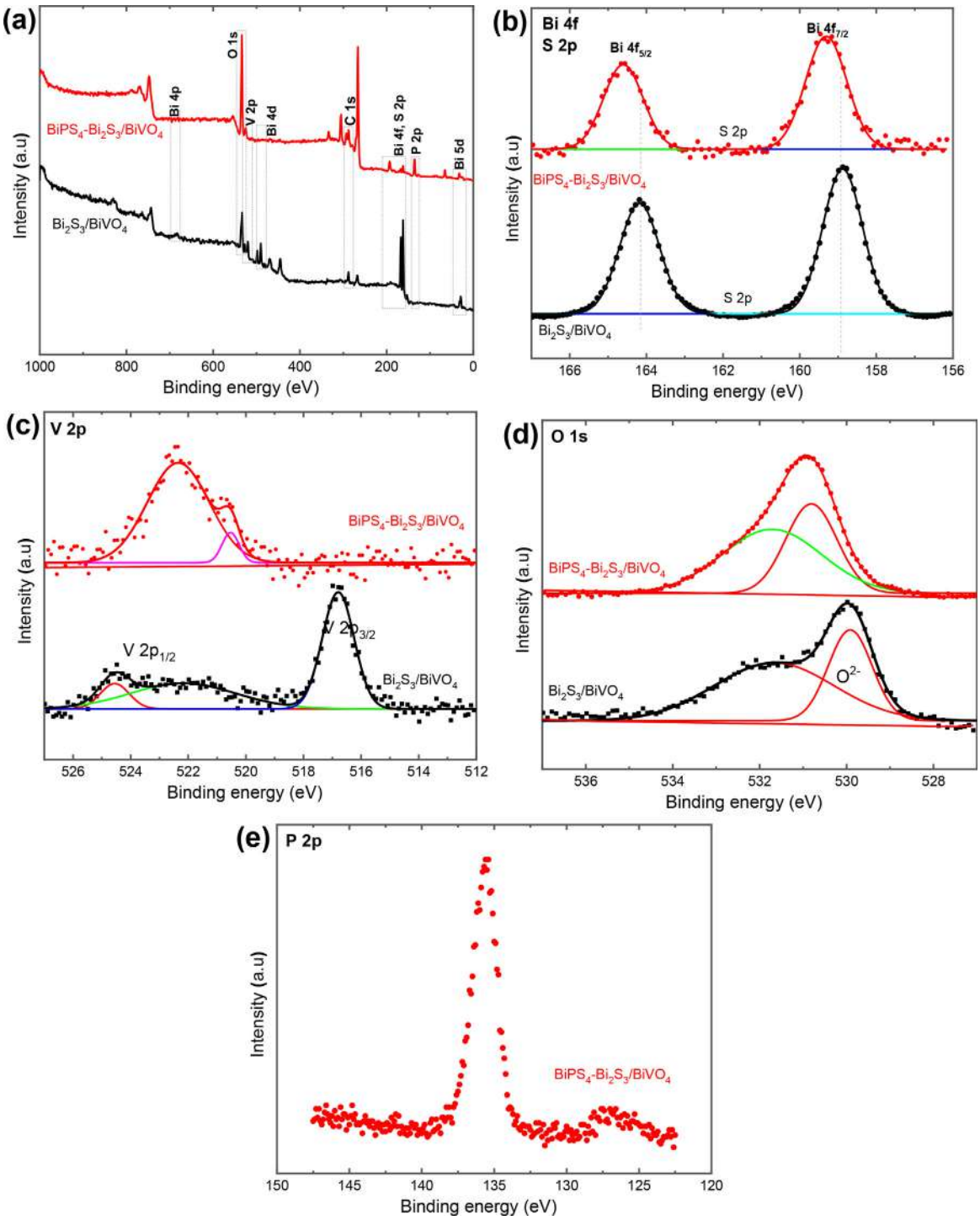

Fig. 4. Surface characterization of photoanodes. Survey XPS spectra of $BiVO_4/Bi_2S_3$-$BiPS_4$and $Bi_2S_3/BiVO_4$ electrodes (a), core level XPS spectra of Bi 4f (b), V 2p (c), O 1 s (d), P 2p (e).

spectrum of $BiVO_4/Bi_2S_3$ photoanodes before the PEC ion-exchange process in 0.1 PBS is included for comparison. The peaks observed at 158.7 and 163.7 eV are splitting peaks of $Bi4f_{7/2}$ and $Bi4f_{5/2}$, individually, which are features of Bi^{3+} (Fig. 4b) [35]. However, the smaller signal at approximately 161.3 eV is attributed to the spin state of S $2p_{1/2}$. Likewise, the obtained peaks positioned at 522.0 ($V2p_{1/2}$) and 516.8 eV ($V2p_{3/2}$) are the splitting peaks of V2p, corresponding to the surface V^{5+} species (Fig. 4c). Furthermore, the acquired peaks at 529.9 and 531.9 eV in the O1s spectrum (Fig. 4d) correspond to O bonded inside an oxide crystal (O^{2-}) in bare-$BiVO_4$ electrodes and to that of adsorbed OH– groups over the electrode surface, correspondingly [48]. More importantly, the high-resolution spectra of Bi (Fig. 4b), V (Fig. 4c), and O (Fig. 4d) of $BiVO_4/Bi_2S_3$-$BiPS_4$ are dissimilar compared to those for $BiVO_4$-Bi_2S_3, with a substantial shift to higher binding energy (BE) in Bi 4f, V2p, and O1s peaks in the heterostructured photoanodes. This evidences an effective efficient monolithic interface between $BiVO_4$ and $BiPS_4$-Bi_2S_3. The higher BE shift is owing to the introduction of sulfur (which has a higher electron affinity) over the VO_4^{3-} tetrahedral sites of $BiVO_4$ [49], consistent with the

Raman analysis above (Fig. 2b) [50]. The HR-XPS spectrum in Fig. 4e displays a P 2p signal at 135.7 eV, assigned to P—O and Bi—P—S combinations. These results indicate that the Bi_2S_3 and $BiPS_4$ nanoparticles were effectively transformed during the PEC transformation process in 0.1 M PBS/Na_2S (pH 10).

3.2. Photoelectrochemical features of photoanodes

A classical 3-electrode assembly was employed for PEC measurements under AM 1.5G simulated sunlight. The highly active $BiVO_4/Bi_2S_3$ heterostructured electrodes from a PEC transformation of $BiVO_4$ in different electrolytes comprising 0.1 M Na_2SO_3/Na_2SO_4 and 0.1 M Na_2S solutions, carried out by varying the number of deposition cycles under light excitations at 100 mW/cm^2. Fig. 5a illustrates the linear sweep voltammogram (LSV) plots of the $BiVO_4/Bi_2S_3$-1 (prepared in 0.1 M Na_2SO_4 + 0.1 M Na_2S electrolytes) photoanodes obtained by different photo deposition cycles in 0.1 M Na_2S/Na_2SO_4 solutions; cycle-10 shows the highest photocurrent, which was selected for fabrication of heterostructured photoanodes. Similarly, the $BiVO_4/Bi_2S_3$-2 electrodes were obtained in the 0.1 Na_2S/Na_2SO_3 solutions, and the results are presented in Fig. 5b. The optimized number of electrochemical cycles for the maximal photocurrent density was 10 cycles. Under light excitation, the enhancement in photocurrent is believed to be due to the PEC transformation, the surface of $BiVO_4$ initiated the transformation into Bi_2S_3 by the diffusion of V-ions into the Na_2S/Na_2SO_3 solution, and the diffusion of Sulfur into the $BiVO_4$lattice [51]. Afterward, the observed photocurrent decrease in the optimal Bi_2S_3 films developed over the $BiVO_4$ surface, which contains the irregular block to the V-leaching process. Further, $BiPS_4$ was decorated over $BiVO_4$ via ion-exchange reactions in an electrolyte comprising 0.1 M PBS and 0.1 M Na_2S solution (Fig. 5c). The PEC conditions for obtaining the best Na_2S/PBS mixing of the nanoparticles were improved by changing electrochemical cycles. Likewise, the addition of $BiPS_4$ on the $BiVO_4/Bi_2S_3$ films was activated under ion-exchange reactions under light excitations, and the $BiVO_4/Bi_2S_3$-$BiPS_4$ (10 cycles) showed the highest PEC performance (Fig. 5c). In addition to the enhanced light absorption, we believe that the integration of $BiVO_4$ and Bi_2S_3-$BiPS_4$ created a triple heterostructured junction, resulting in more efficient photoinduced carrier separation and declined charge recombination[52–53].

The distinctive photocurrent–potential (J–V) schemes for the PEC water splitting reaction in Fig. 6a show that the optimal $BiVO_4/Bi_2S_3$-$BiPS_4$ photoanodes presented superior photocurrents to $BiVO_4/Bi_2S_3$-1 and $BiVO_4/Bi_2S_3$-2. The high onset potential (0.85 V_{RHE}) and lower photocurrent response of the bare-$BiVO_4$ (≈0.7 mA/cm^2 at 1.23 V_{RHE}) are apparently credited to the poor hole transfer kinetics at the interface between the bare $BiVO_4$ and water [54]. The photocurrent density upsurged from 1.97 to 3.7 mA/cm^2 after introducing the $BiPS_4$ layer owing to enriched light absorption and, successively, enhanced photoinduced carrier generation. Further, the photocurrent density considerably upsurged with Bi_2S_3-$BiPS_4$ decoration and attained ~3.7 mA/cm^2 at 1.23 V_{RHE} in 0.1 M PBS/Na_2S (pH 10), which is nearly a 5-fold enrichment compared to bare $BiVO_4$. The photocurrent onset potentials (V_{on}) for the fabricated heterostructured electrodes were estimated from the quasi-steady-state J–V schemes acquired at a photocurrent density of 1 mA/cm^2, and the estimated values were 0.25 V_{RHE} for $BiVO_4/Bi_2S_3$-$BiPS_4$ compared 0.85 V_{RHE} for $BiVO_4$ (Fig. 6a). Compared to the other samples, a superior photocurrent density was achieved in the lower potential area (0.6 V_{RHE}). Based on this fact, it is obvious that a transformation toward $BiPS_4$ and Bi_2S_3 films is mandatory to justify the demand for higher efficiency as well as durability. For estimating the ABPE efficiencies of the heterostructured electrodes, the raw data were obtained from Fig. 6a, and are presented in Fig. 6b. The maximal photoconversion efficiency of the fabricated $BiVO_4/Bi_2S_3$-$BiPS_4$ heterostructured photoanode is (1.40 % at 0.60 V_{RHE}), which is substantially nearly 2-fold enhancement compared to the $BiVO_4/Bi_2S_3$-1 photoanode (0.79 % at 0.6 V_{RHE}) and $BiVO_4/Bi_2S_3$-1 photoanode (0.81 % at 0.6 V_{RHE}). Fig. 6c displays the chopped LSVs of the $BiVO_4/Bi_2S_3$-$BiPS_4$, $BiVO_4/Bi_2S_3$-1, $BiVO_4$/ Bi_2S_3-2 at 5 mV/s under pulsed light irradiation in 0.1 M Na_2S/PBS solution (pH ~ 10). Fig. 6e showed the linear relationship between $\Delta J = (J_a\text{-}J_c)$ at + 1.23 V_{RHE} and the sweep rates; from the slope of the linear fit, the C_{dl} was estimated and shown in Table 1, which is openly related to the electrochemically active surface area of the materials [55]. The $BiVO_4/Bi_2S_3$-$BiPS_4$ electrodes (52.65 μF/cm^2) have a higher C_{dl}, which is a 3-fold enhancement than the bare $BiVO_4$ (19.6 μF/cm^2), which evidences that the integration of Bi_2S_3-$BiPS_4$ over the surface of the $BiVO_4$ advances the active surface area and develops more active sites for water oxidation. Comparatively, a superior photocurrent density was acquired $BiVO_4/Bi_2S_3$-$BiPS_4$ in the lower potential part (0.6 V_{RHE}) than the other electrodes (Fig. 6f), which is remarkable for developing tandem photoanode-photocathode arrangements.

The dynamics of charge transfer features of the heterostructured electrodes were explored by EIS under visible-light excitation. The Nyquist curve of the $BiVO_4/Bi_2S_3$-$BiPS_4$ electrodes evaluated under visible-light excitation at 0.65 V_{RHE} and the matching equivalent circuit are exhibited in Fig. 7a. Notably, these results validate that the diameter of the arc on the $BiVO_4/Bi_2S_3$-$BiPS_4$ heterostructured photoanodes was lower than that of $BiVO_4$/ Bi_2S_3 electrodes. The smaller arc radius of the $BiVO_4/Bi_2S_3$-$BiPS_4$ electrodes suggests faster interfacial charge transfer than bare $BiVO_4$. Notably, the fabricated $BiVO_4/Bi_2S_3$-$BiPS_4$ heterostructured electrode shows the smallest R_{ct} value (**Table S1**). The constant capacitance and reduction in the charge transfer resistance (R_{CT}) at similar voltages reveal that $BiPS_4$ functioned as an efficient film, boosting the charge transfer kinetics and reducing surface recombination. These results validate that the PEC surface transformation of $BiVO_4$ to Bi_2S_3-$BiPS_4$ can reduce the R_{CT} considerably, due to the development of a triple $BiPS_4$/ Bi_2S_3/ $BiVO_4$ heterostructured interface system.

Fig. 7b demonstrates the corresponding Bode phase curves of the $BiVO_4$, $BiVO_4/Bi_2S_3$, and $BiVO_4/Bi_2S_3$-$BiPS_4$, which explains the kinetics of the electrochemical reaction on the electrode surface [56]. The higher frequency of the $BiVO_4/Bi_2S_3$-$BiPS_4$ submits the quicker water oxidation kinetics via the rapid hole transfer process. Moreover, the hole relaxation lifetime (τ_p) was estimated from the Bode phase plot and provided in Table 1. The smallest τ_p of the $BiVO_4/Bi_2S_3$-$BiPS_4$ photoanode evidence the rapid hole-consumed water oxidation process. Likewise, from τ_p, the hole diffusion length of the $BiVO_4$ and $BiVO_4/Bi_2S_3$-$BiPS_4$ photoanodes is also derived and given in Table 1, supporting the greater hole consumed water oxidation kinetics in $BiVO_4/Bi_2S_3$-$BiPS_4$ than $BiVO_4$ [57]. All the acquired results noticeably show that the transformation of both Bi_2S_3 and $BiPS_4$ over $BiVO_4$ electrodes influences the PEC features deeply.

The long-term durability of the heterostructured electrode was inspected by chronoamperometric measurements. Fig. 8a displays the long-standing durability of $BiVO_4/Bi_2S_3$-$BiPS_4$ at 0.8 V_{RHE} built on the J–t plots obtained in 0.1 M PBS/Na_2S over 10 h, at a photocurrent response of ~3.4 mA/cm^2; there was no apparent decay, demonstrating the remarkable durability with the integration of $BiPS_4$ under continuous illumination. Particularly, the obtained photocurrent parameters agreed with the results acquired from the equivalent LSV curves. The heterostructured $BiVO_4/Bi_2S_3$-$BiPS_4$ heterostructured photoanodes, which exhibit the synergetic effect of both Bi_2S_3 and $BiPS_4$, exhibited a faster decline of photocurrent at first and could withstand a substantial photocurrent density after 7 h of about 2.84 mA/cm^2, which is ~ 84 % of its initial

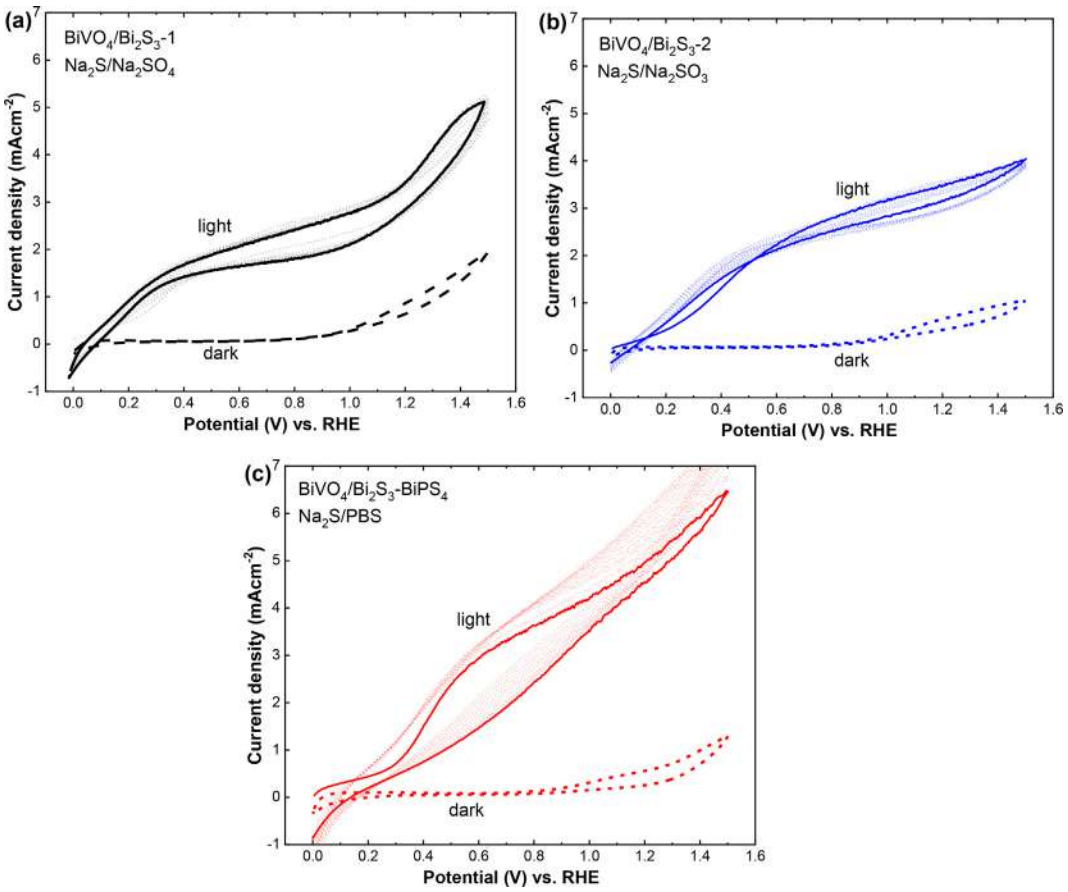

Fig. 5. Effect of electrolytes on the PEC activity of $BiVO_4$ electrodes. (a) CV characteristics of $BiVO_4/Bi_2S_3$-1 photoanodes prepared in 0.1 M Na_2SO_4 + 0.1 M Na_2S electrolytes (pH 10) under visible light excitations conditions (100 mW/cm^2) for continuous 10 cycles, (b) CV characteristics of $BiVO_4/Bi_2S_3$-2 photoanodes prepared using 0.1 M Na_2S/Na_2SO_3 electrolyte (pH 10) under irradiation of and (c) CV characteristics of $BiVO_4/Bi_2S_3$-$BiPS_4$ photoanodes prepared through 0.1 M Na_2S + 0.1 M PBS electrolyte (pH 10) under light excitations. Dark (dashed line), Light (dotted line), after continuous cycles (solid line).

value. However, the J-t profile of $BiVO_4/Bi_2S_3$-$BiPS_4$ ultimately revealed better durability compared to that of $BiVO_4/Bi_2S_3$ after 10 h of testing, as can be revealed from the enlarged J-t plot in Fig. 8b. Moreover, the $BiVO_4/Bi_2S_3$-$BiPS_4$ heterostructured photoanodes present less spikes on the photocurrent than the $BiVO_4/Bi_2S_3$ photoanodes. These results validate the suppressed charge recombination sites for the photoanodes with the introduction of $BiPS_4$. In addition, the photoelectrochemically transformed $BiPS_4$ layer over the $BiVO_4$ surface will generate additional photoinduced charge carriers with an additional type II $Bi_2S_3/BiPS_4$ heterojunction for efficient charge separation. Our results, therefore, validate the function of the transformed electrodes in suppressing the charge recombination and boosting the PEC features at the same time [58]. Table 2 relates the photoanodes fabricated in the present work with those stated earlier in the literature. The results designate that our $BiVO_4/Bi_2S_3$-$BiPS_4$ heterostructured electrodes are durable and efficient for oxidizing water into O_2.

Photoelectrochemical production of OER via photoelectrocatalysis at $BiVO_4/Bi_2S_3$ and $BiVO_4/Bi_2S_3$-$BiPS_4$ films were observed through an Oxysense instrument. **Figure S1** shows the evidence of O_2 evolution concentration with respect to the time for triple-layered $BiVO_4/Bi_2S_3$-$BiPS_4$ electrodes at 0.6 V_{RHE} and with continuous illumination. As observed in the figures, after $BiPS_4$ addition, visible-light photons ($\lambda > 420$ nm) insisted dioxygen evolution over the electrode surface of $BiVO_4/Bi_2S_3$-$BiPS_4$, and their matching photocurrent analysis is shown in Fig. S1b. With the aid of potential (0.6 V_{RHE}), dioxygen generation was detected, and their acquired concentrations were expected to increase linearly with time intervals. On the other hand, the obtained $BiVO_4/Bi_2S_3$-$BiPS_4$ electrodes evidenced considerable durability towards continuous illumination conditions (Fig. S1b). All the acquired results evidence that the synergetic effect of $BiPS_4$ and Bi_2S_3 transformation considerably boosted the PEC performances and durability of $BiVO_4$ electrodes by improving the charge-carrier density and the surface oxidation kinetics.

Generally, the PEC features of prepared electrode materials rely mainly on their energy band structures [70]. The energy level positions of the conduction and valence band can be predicted by the following equations [71]

$$E_{CB} = X - E_e - 0.5E_g \quad (1)$$

$$E_{VB} = E_{CB} + E_g \quad (2)$$

where X and E_g are the absolute electronegativity and the bandgap of the materials, correspondingly. E_e is the energy of a free electron on the hydrogen scale (4.5 eV). The X values for bare $BiVO_4$, Bi_2S_3, and $BiPS_4$ are 6.04 [72], 5.26 [73], and 5.31 eV, individually. The acquired bandgap parameters for $BiVO_4$, Bi_2S_3, and $BiPS_4$ have been assessed to be 2.4, 1.39, and 1.30 eV, correspondingly (**Figure S2**). Hence, the obtained ECB values of $BiVO_4$, Bi_2S_3, and $BiPS_4$ are assessed to be 0.34, 0.065, and 0.11 eV, individually. The E_{VB} values of $BiVO_4$, Bi_2S_3, and $BiPS_4$ can be assessed to be 2.74, 1.455, and 1.41 eV, respectively. These data determinations might assist to discuss the relative determinations of their energy bands (**Figure S3**). Notably, Fig. 9 illustrates the proposed mechanism of $BiVO_4/Bi_2S_3$-$BiPS_4$ heterostructured photoanode under

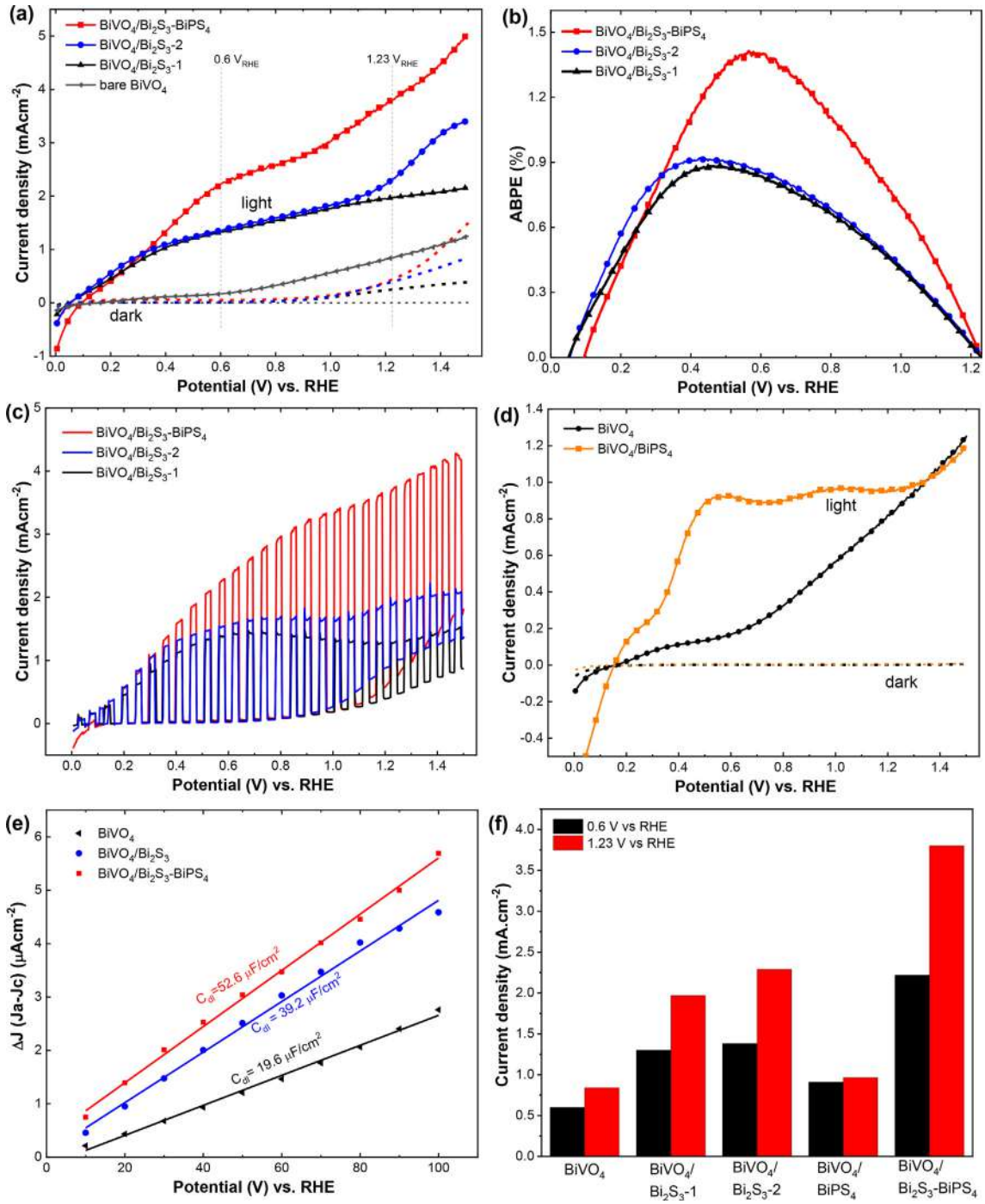

Fig. 6. (a) Polarization curves for $BiVO_4$, $BiVO_4/Bi_2S_3$-1 (0.1 M Na_2SO_4/0.1 M Na_2S), $BiVO_4/Bi_2S_3$-2 (0.1 M Na_2SO_3/0.1 M Na_2S) and $BiVO_4/Bi_2S_3$-$BiPS_4$ using a 0.1 M Na_2S and 0.1 M PBS, (b) estimated ABPE efficiency, (c) corresponding chopped polarization curves in 0.1 M PBS, and (d) polarization curves in the dark (black) and under irradiation (orange) for $BiVO_4/BiPS_4$ and (e) curves of ΔJ at 1.23 V_{RHE} vs sweep rates; LSV curves of the obtained electrode (f) Variation in the photocurrent density for all fabricated materials in 0.1 M PBS and 0.1 M Na_2S (pH 10) at 0.6 and 1.23 V_{RHE}. (For interpretation of the references to colour in this figure legend, the reader is referred to the web version of this article.)

illumination conditions. Particularly, the photoinduced holes in the valence band of bare-$BiVO_4$ electrodes interact with the SO_3^{2-}/S^{2-} radicals in the presence of Na_2S/Na_2SO_3 sacrificial reagents and oxidize to develop S_2^{2-} and $S_2O_3^{2-}$. Simultaneously, S^{2-} ion effectively interacts with bare-$BiVO_4$ and produces Bi_2S_3 at the surface of $BiVO_4$. Firstly, the $BiVO_4$ film facilitates direct electron transfer, whereas Bi_2S_3 assists as the front light absorber. As defined in the energy level band diagram of Fig. 9, the photogenerated electrons in the CB of Bi_2S_3 transfer to the CB of $BiVO_4$, and meanwhile the photoinduced electrons are produced in the CB of $BiVO_4$ itself. Simultaneously, the photoinduced holes in the VB of $BiVO_4$ will effectively transport to the VB of Bi_2S_3 owed to the built-in electric field developed by the type II heterojunction [65,74]. In a nutshell, electrons and holes will be produced in both materials, and the type II structure of the interface will drive electrons toward $BiVO_4$ and holes toward the water interface. The same can be mentioned for the additional $BiPS_4$ later in the triple structure. The three materials $BiVO_4$, Bi_2S_3, and $BiPS_4$ make perfect valence band energy

Table 1
PEC values were acquired for the $BiVO_4$, $BiVO_4/Bi_2S_3$ and $BiVO_4/Bi_2S_3$-$BiPS_4$ electrodes.

Photoanode	J_{H2O} ($mA.cm^{-2}$) @1.23 V_{RHE}	ABPE (%)	R_{CT} (Ω)	C_{dl} ($\mu F.cm^{-2}$)	Relaxation frequency (Hz)	τ_p (ms)	L_D (μm)
$BiVO_4$	0.85	–	1.1 E^{12}	19.6	4.624	34.43678	423.2
$BiVO_4/Bi_2S_3$	1.97	0.89	6351	39.2	9.521	16.72468	294.9
$BiVO_4/Bi_2S_3$-$BiPS_4$	3.85	1.41	456.1	52.6	15.346	10.37636	232.3

Footnote: J_{H2O} referring to the photocurrent density; ABPE - Applied bias photon-to-current efficiency; C_{dl} - Double-layer capacitance; τ_p –hole relaxation lifetime; L_D- hole diffusion length;

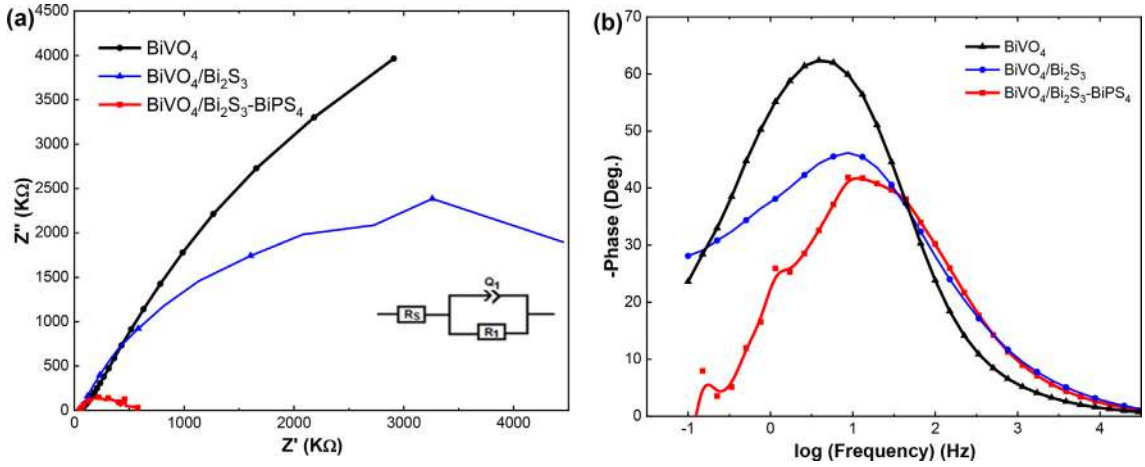

Fig. 7. Impedance spectra of photoanodes. Comparative Nyquist plots (a) and its corresponding Bode phase plots (b) for $BiVO_4$ (black), $BiVO_4/Bi_2S_3$ (blue) (tested in 0.1 M Na_2SO_3 + 0.1 M Na_2S), and $BiVO_4/Bi_2S_3$-$BiPS_4$ (red) (tested in 0.1 M PBS + 0.1 M Na_2S) (red) photoanodes at 1.23 V_{RHE} with a frequency ranging between 100,000 to 0.05 Hz under visible-light excitations. Inset displays fitted equivalent circuits for the photoanodes. (For interpretation of the references to colour in this figure legend, the reader is referred to the web version of this article.)

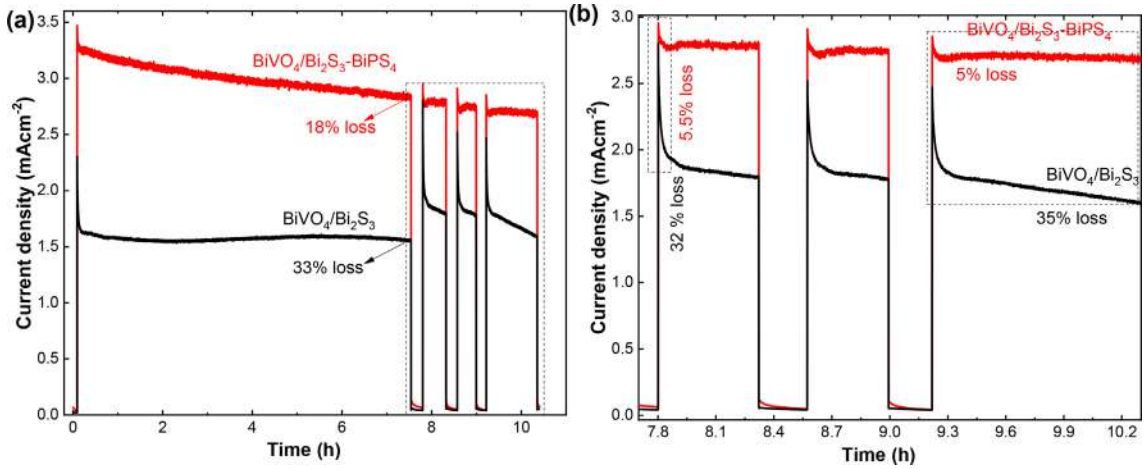

Fig. 8. (a) J–t curve for long-term photodurability of $BiVO_4/Bi_2S_3$-$BiPS_4$ (tested in 0.1 M PBS + M 0.1 Na_2S) (red) and $BiVO_4/Bi_2S_3$ (tested in 0.1 M Na_2SO_3 + Na_2S) (black) at 0.8 V_{RHE} for ~ 10 h under AM 1.5 G irradiation. (b) enlarged view of prepared electrodes. (For interpretation of the references to colour in this figure legend, the reader is referred to the web version of this article.)

alignment for the efficient extraction of holes towards the water interface. Therefore, we have two types II heterojunctions and three absorbing materials. Hence, light absorption will be magnified and the charge transfer kinetics will be facilitated at the same time, explaining the large enhancement in the triple electrode. Hence, this triple-layer heterostructured $BiVO_4/Bi_2S_3$-$BiPS_4$ configuration can be an effective water oxidation process. These results provide basic knowledge and design of effective heterostructured photoanodes for solar fuel production.

4. Conclusions

In summary, a noble $BiVO_4/Bi_2S_3$-$BiPS_4$ electrode was fabricated on a conducting substrate via the PEC ion exchange process. Initially, homogeneous $BiVO_4/Bi_2S_3$ particles are synthesized by the PEC transformation process in an aqueous Na_2S/Na_2SO_3 electrolyte and then subjected to the PEC -ion exchange process to produce $BiVO_4/Bi_2S_3$-$BiPS_4$ electrode in Na_2S/PBS electrolyte. When the surface of $BiVO_4$ was transformed with the Bi_2S_3-$BiPS_4$ layer, the resulting $BiVO_4/Bi_2S_3$-$BiPS_4$ heterostructured electrodes demon-

Table 2
Various kinds of $BiVO_4$-based electrode materials are loaded with different co-catalysts and their PEC properties for water-splitting reactions.

S.No	Electrode	Electrolyte (pH)	Co-catalyst (Method)	Light source	Current density (mA/cm^2)	Ref.
1	$BiVO_4/FeVO_4$	0.2 M Na_2SO_4 pH = 7	Electrospray technique	100 $mW.cm^{-2}$	0.4 @ 1.23 V_{RHE}	[59]
2	$BiVO_4$/CoFe-NiOOH	0.5 M Na_2SO_4 pH = 7	Lifting method/chemical process	100 mW/cm^2	1.54 @ 1.23 V_{RHE}	[60]
3	$BiVO_4$/rGO/NiFe	0.5 M Na_2SO_4 pH = ~6.9	Potentiostatic electrodeposition	100 $mW.cm^{-2}$	1.30 @ 1.23 V_{RHE}	[61]
4	BiVO4/Ni0.5Fe0.5-LDH	0.5 M Na_2SO_4	Electrodeposition process	100 $mW.cm^{-2}$	1.21 @ 1.23 V_{RHE}	[62]
5	CoPi/$BiVO_4$	0.5 M Na_2SO_4	Photodeposition	100 $mW.cm^{-2}$	1.1 @ 1.23 V_{RHE}	[63]
6	CoFe-PB/$BiVO_4$	0.1 M KPi	Wet processing method	100 $mW.cm^{-2}$	1.0 @ 1.23 V_{RHE}	[64]
7	Ag/Ni-Zr:$BiVO_4$	0.1 M PBS pH 7.5	Electrochemical deposition process	100 $mW.cm^{-2}$	3.14 @1.23 V_{RHE}	[26]
8	NiFePB/Zr:$BiVO_4$	0.1 M PBS pH 7.5	Electrodeposition process	100 $mW.cm^{-2}$	3.23 @1.23 V_{RHE}	[25]
9	$BiVO_4/Bi_2S_3$	0.5 M Na_2SO_4	Photoassisted electrodeposition process	100 $mW.cm^{-2}$	1.43 @1.23 V_{RHE}	[35]
10	$BiVO_4/Bi_2S_3$	0.35 M Na_2SO_3/0.25 M Na_2S	PEC transformation	100 $mW.cm^{-2}$	3.3 @1.23 V_{RHE}	[65]
11	$BiVO_4/Bi_2S_3$/FeOOH	0.1 M Na_2SO_4	Hydrothermal process	100 $mW.cm^{-2}$	0.8 @0.4 V_{SCE}	[66]
12	Mo:$BiVO_4$	0.1 M Na_2SO_4	Pulsed laser deposition	100 $mW.cm^{-2}$	2.1@1.23 V_{RHE}	[67]
13	$BiVO_4$/V-NiOOH/FeOOH	1 M KBi	Hydrothermal method	100 $mW.cm^{-2}$	5.43 @ 1.23 V_{RHE}	[68]
14	Activated EL-$BiVO_4$	1 M KBi	In-situ potentiostatic photopolarisation	100 $mW.cm^{-2}$	4.6 @1.23 V_{RHE}	[69]
13	$BiVO_4/Bi_2S_3$	0.1 M PBS/Na_2S pH 10	Ion-exchange reactions	AM 1.5G/100 mW/cm^2	1.97 @1.23 V_{RHE}	This work
14	$BiVO_4/Bi_2S_3/BiPS_4$	0.1 M PBS/Na_2S pH 10	Ion-exchange reactions	AM 1.5G/100 mW/cm^2	3.85 @1.23 V_{RHE}	This work

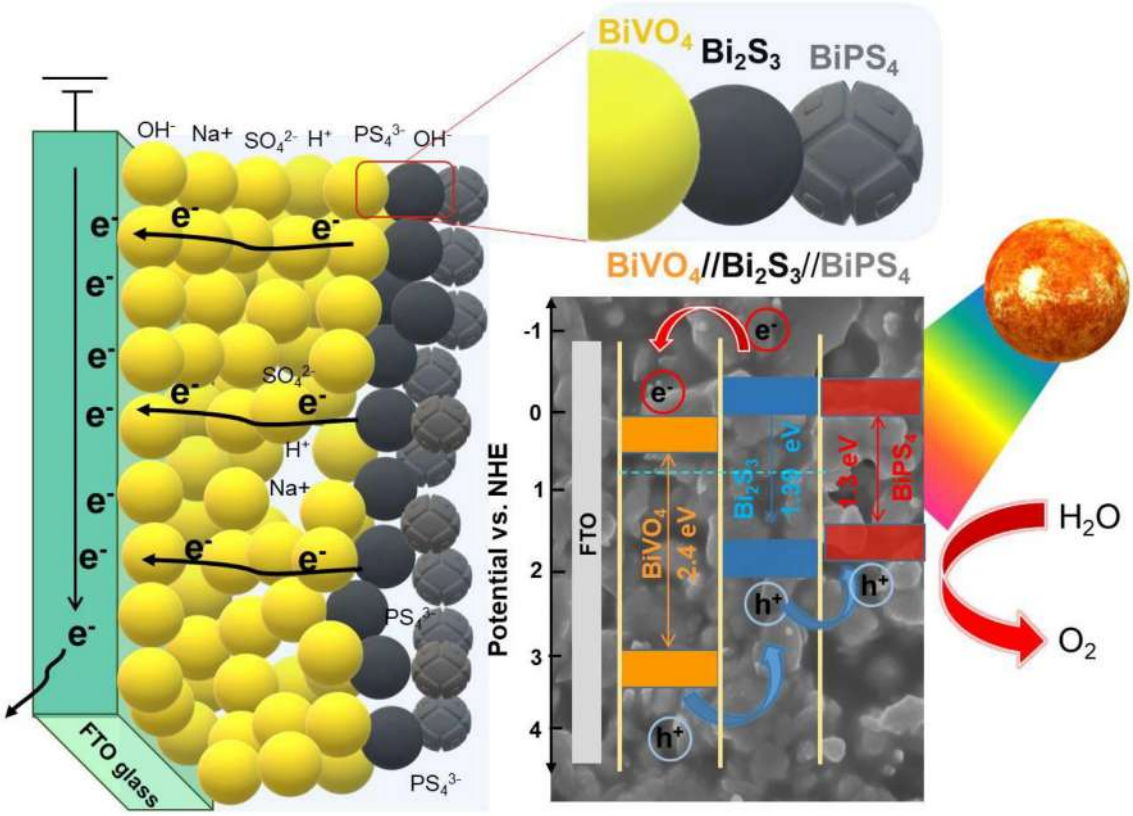

Fig. 9. Mechanistic illustration of $BiVO_4/Bi_2S_3$-$BiPS_4$ heterostructured electrode and its energy level diagrams under irradiation for the electrodes and electrolyte interface.

strated superior photocurrent features of ~3.7 mA/cm^2 at 1.23 V_{RHE}. The impedances and absorption spectra show that the $BiPS_4$ layer assists as a surface protective film and boosts the PEC features by upsurging the photon absorption and carrier separation of the $BiVO_4$ film. The exceptional PEC feature and durability and the rapid, convenient, and well-regulated commercial fabrication

of the $BiPS_4$ photoanodes make it a favorable substitute for conventional metal oxide-protected water-splitting photoanodes.

CRediT authorship contribution statement

Maged N. Shaddad: Conceptualization, Data curation, Formal analysis, Investigation. **Prabhakarn Arunachalam:** Conceptualization, Data curation, Formal analysis, Investigation, Supervision, Writing – original draft, Writing – review & editing. **Mahmoud Hezam:** Investigation, Conceptualization, Writing – review & editing. **Norah M BinSaeedan:** Formal analysis. **Sixto Gimenez:** Supervision. **Juan Bisquert:** Supervision. **Abdullah M. Al-Mayouf:** Supervision, Funding acquisition, Project administration.

Data availability

Data will be made available on request.

Declaration of Competing Interest

The authors declare that they have no known competing financial interests or personal relationships that could have appeared to influence the work reported in this paper.

Acknowledgments

This project was funded by the National Plan for Science, Technology and Innovation, King Abdulaziz City for Science and Technology, Kingdom of Saudi Arabia, Award Number (14-NAN2323-02).

Appendix A. Supplementary material

Supplementary data to this article can be found online at https://doi.org/10.1016/j.jcat.2022.12.032.

References

[1] S. Dutta, Review on Solar Hydrogen: Its Prospects and Limitations, Energy Fuel 35 (2021) 11613–11639, https://doi.org/10.1021/acs.energyfuels.1c00823.
[2] C. Acar, I. Dincer, G.F. Naterer, Review of Photocatalytic Water-splitting Methods for Sustainable Hydrogen Production, Int. J. Energy Res. 40 (2016) 1449–1473, https://doi.org/10.1002/er.3549.
[3] F. Li, C.L. Wang, S. Ding, K. Yang, C.J. Liu, F. Tian, Photoelectrochemical performance of TiO2 nanotube arrays by in situ decoration with different initial states, Rare Met. 40 (2021) 720–727, https://doi.org/10.1007/s12598-019-01363-7.
[4] J.H. Kim, J.W. Jang, Y.H. Jo, F.F. Abdi, Y.H. Lee, R. Van De Krol, J.S. Lee, Hetero-type dual photoanodes for unbiased solar water splitting with extended light harvesting, Nat. Commun. 7 (2016) 1–9, https://doi.org/10.1038/ncomms13380.
[5] X. Liu, F. Wang, Q. Wang, Nanostructure-based WO3 photoanodes for photoelectrochemical water splitting, PCCP 14 (2012) 7894–7911, https://doi.org/10.1039/C2CP40976C.
[6] S.W. Hwang, D.H. Seo, J.U. Kim, D.K. Lee, K.S. Choi, C. Jeon, I.S. Cho, Bismuth vanadate photoanode synthesized by electron-beam evaporation of a single precursor source for enhanced solar water-splitting, Appl. Surf. Sci. 528 (2020), https://doi.org/10.1016/j.apsusc.2020.146906.
[7] Y. Peng, H. Wu, M. Yuan, F. F., Li, X. Zou, Y. H. Ng, H. Y. Hsu,, Chemical reduction-induced surface oxygen vacancies of BiVO 4 photoanodes with enhanced photoelectrochemical performance, Sustainable Energy & Fuels 5 (2021) 2284–2293, https://doi.org/10.1039/D0SE01901A.
[8] M.N. Shaddad, M.A. Ghanem, A.M. Al-Mayouf, S. Gimenez, J. Bisquert, I. Herraiz-Cardona, Cooperative Catalytic Effect of ZrO2 and α-Fe2O3 Nanoparticles on BiVO4 Photoanodes for Enhanced Photoelectrochemical Water Splitting, ChemSusChem 9 (2016) 2779–2783, https://doi.org/10.1002/cssc.201600890.
[9] J.H. Kim, J.S. Lee, Elaborately modified BiVO4 photoanodes for solar water splitting, Adv. Mater. 31 (2019) 1806938, https://doi.org/10.1002/adma.201806938.
[10] V. Nair, C.L. Perkins, Q. Lin, M. Law, Textured nanoporous Mo: BiVO 4 photoanodes with high charge transport and charge transfer quantum efficiencies for oxygen evolution, Energ. Environ. Sci. 9 (2016) 1412–1429, https://doi.org/10.1039/C6EE00129G.
[11] H.L. Tan, X. Wen, R. Amal, Y.H. Ng, BiVO4 010 and 110 relative exposure extent: governing factor of surface charge population and photocatalytic activity, The Journal of Physical Chemistry Letters 7 (2016) 1400–1405, https://doi.org/10.1021/acs.jpclett.6b00428.
[12] D.K. Zhong, S. Choi, D.R. Gamelin, Near-complete suppression of surface recombination in solar photoelectrolysis by "Co-Pi" catalyst-modified W: BiVO4, J. Am. Chem. Soc. 133 (2011) 18370–18377, https://doi.org/10.1021/ja207348x.
[13] T. Liu, X. Zhou, M. Dupuis, C. Li, The nature of photogenerated charge separation among different crystal facets of BiVO4 studied by density functional theory, PCCP 17 (2015) 23503–23510, https://doi.org/10.1039/C5CP04299B.
[14] R. Guo, A. Yan, J. Xu, B. Xu, T. Li, X. Liu, S. Luo, Effects of morphology on the visible-light-driven photocatalytic and bactericidal properties of BiVO4/CdS heterojunctions: A discussion on photocatalysis mechanism, J. Alloy. Compd. 817 (2020), https://doi.org/10.1016/j.jallcom.2019.153246.
[15] M.N. Shaddad, P. Arunachalam, M. Hezam, N.M. AL-Saeedan, S. Gimenez, J. Bisquert, A.M. Al-Mayouf,, Unprecedented solar water splitting of dendritic nanostructured Bi2O3 films by combined oxygen vacancy formation and Na2MoO4 doping, Int. J. Hydrogen Energy 46 (2021) 23702–23714, https://doi.org/10.1016/j.ijhydene.2021.04.184.
[16] H.S. Park, K.E. Kweon, H. Ye, E. Paek, G.S. Hwang, A.J. Bard, Factors in the metal doping of BiVO4 for improved photoelectrocatalytic activity as studied by scanning electrochemical microscopy and first-principles density-functional calculation, J. Phys. Chem. C 115 (2011) 17870–17879, https://doi.org/10.1021/jp204492r.
[17] S.K. Pilli, T.E. Furtak, L.D. Brown, T.G. Deutsch, J.A. Turner, A.M. Herring, Cobalt-phosphate (Co-Pi) catalyst modified Mo-doped BiVO 4 photoelectrodes for solar water oxidation, Energ. Environ. Sci. 4 (2011) 5028–5034, https://doi.org/10.1039/C1EE02444B.
[18] H. Xu, W. Fan, Y. Zhao, B. Chen, Y. Gao, X. Chen, D. Xu, W. Shi, Amorphous iron (III)-borate decorated electrochemically treated-BiVO4 photoanode for efficient photoelectrochemical water splitting, Chem. Eng. J. 411 (2021), https://doi.org/10.1016/j.cej.2021.128480.
[19] T.W. Kim, K.S. Choi, Nanoporous BiVO4 photoanodes with dual-layer oxygen evolution catalysts for solar water splitting, Science 343 (2014) 990–994, https://doi.org/10.1126/science.1246913.
[20] Z. Sun, Z. Yu, Y. Liu, C. Shi, M. Zhu, A. Wang, Construction of 2D/2D BiVO4/g-C3N4 nanosheet heterostructures with improved photocatalytic activity, J. Colloid Interface Sci. 533 (2019) 251–258, https://doi.org/10.1016/j.jcis.2018.08.071.
[21] Y. Wu, J. Wang, Y. Huang, Y. Wei, Z. Sun, X. Zheng, J. Wu, Solvothermal synthesis of Bi2O3/BiVO4 heterojunction with enhanced visible-light photocatalytic performances, J. Semicond. 37 (2016), https://doi.org/10.1088/1674-4926/37/8/083004.
[22] S.Y. Chae, C.S. Lee, H. Jung, O.S. Joo, B.K. Min, J.H. Kim, Y.J. Hwang, Insight into charge separation in WO3/BiVO4 heterojunction for solar water splitting, ACS Appl. Mater. Interfaces 9 (2017) 19780–19790, https://doi.org/10.1021/acsami.7b02486.
[23] C. Regmi, D. Dhakal, T.H. Kim, T. Yamaguchi, S.W. Lee, Fabrication of Ag-decorated BiOBr-mBiVO4 dual heterojunction composite with enhanced visible light photocatalytic performance for degradation of malachite green, Nanotechnology 29 (2018), https://doi.org/10.1088/1361-6528/aaac60.
[24] M.N. Shaddad, D. Cardenas-Morcoso, P. Arunachalam, M. García-Tecedor, M.A. Ghanem, J. Bisquert, S. Gimenez, Enhancing the optical absorption and interfacial properties of BiVO4 with Ag3PO4 nanoparticles for efficient water splitting, J. Phys. Chem. C 122 (2018) 11608–11615, https://doi.org/10.1021/acs.jpcc.8b00738.
[25] M.N. Shaddad, P. Arunachalam, J. Labis, M. Hezam, A.M. Al-Mayouf, Fabrication of robust nanostructured (Zr) BiVO4/nickel hexacyanoferrate core/shell photoanodes for solar water splitting, Appl Catal B 244 (2019) 863–870, https://doi.org/10.1016/j.apcatb.2018.11.079.
[26] M.N. Shaddad, P. Arunachalam, A.A. Alothman, A.M. Beagan, M.N. Alshalwi, A. M. Al-Mayouf, Synergetic catalytic behavior of AgNi-OH-Pi nanostructures on Zr: BiVO4 photoanode for improved stability and photoelectrochemical water splitting performance, Journal of Catalysis 371 (2019) 10–19, https://doi.org/10.1016/j.jcat.2019.01.024.
[27] M.N. Shaddad, P. Arunachalam, M. Hezam, A.M. Al-Mayouf, Cooperative catalytic behavior of SnO2 and NiWO4 over BiVO4 photoanodes for enhanced photoelectrochemical water splitting performance, Catalysts 9 (2019) 879, https://doi.org/10.3390/catal9110879.
[28] M. Sun, C. Yuan, R.T. Gao, R. Zhang, X. Liu, T. Nakajima, L. Wang, A bridging coordination of urea tailoring metal hydroxides oxygen evolution catalysts promotes stable solar water splitting, Chem. Eng. J. 426 (2021), https://doi.org/10.1016/j.cej.2021.131062.
[29] Z. Najaf, D.L.T. Nguyen, S.Y. Chae, O.S. Joo, A.U.H.A. Shah, D.V.N. Vo, G. Rahman, Recent trends in development of hematite (α-Fe2O3) as an efficient photoanode for enhancement of photoelectrochemical hydrogen production by solar water splitting, Int. J. Hydrogen Energy 46 (2021) 23334–23357, https://doi.org/10.1016/j.ijhydene.2020.07.111.
[30] Y. Ma, A. Kafizas, S.R. Pendlebury, F. Le Formal, J.R. Durrant, Photoinduced absorption spectroscopy of CoPi on BiVO4: the function of CoPi during water oxidation, Adv. Funct. Mater. 26 (2016) 4951–4960, https://doi.org/10.1002/adfm.201600711.
[31] Y. Ma, F. Le Formal, A. Kafizas, S.R. Pendlebury, J.R. Durrant, Efficient suppression of back electron/hole recombination in cobalt phosphate

surface-modified undoped bismuth vanadate photoanodes, J. Mater. Chem. A 3 (2015) 20649–20657, https://doi.org/10.1039/C5TA05826K.
[32] Y. Wan, M. Han, L. Yu, G. Yi, J. Jia, 3D Bi 2 S 3 salix leaf-like nanosheet/TiO2 nanorod branched heterostructure arrays for improving photoelectrochemical properties, CrstEngComm 18 (2016) 1577–1584, https://doi.org/10.1039/C5CE02252E.
[33] C. Liu, J. Li, Y. Li, W. Li, Y. Yang, Q. Chen, Epitaxial growth of Bi 2 S 3 nanowires on BiVO4 nanostructures for enhancing photoelectrochemical performance, RSC Adv. 5 (2015) 71692–71698, https://doi.org/10.1039/C5RA13171E.
[34] Z. Zhou, Y. Li, K. Lv, X. Wu, Q. Li, J. Luo, Fabrication of walnut-like BiVO4@ Bi2S3 heterojunction for efficient visible photocatalytic reduction of Cr (VI), Mater. Sci. Semicond. Process. 75 (2018) 334–341, https://doi.org/10.1016/j.mssp.2017.11.011.
[35] H.Q. Chen, L.Y. Lin, S.L. Chen, Direct growth of BiVO4/Bi2S3 nanorod array on conductive glass as photocatalyst for enhancing the photoelectrochemical performance, ACS Applied Energy Materials 1 (2018) 6089–6100, https://doi.org/10.1021/acsaem.8b01146.
[36] D. Tiwari, D. Alibhai, D. Cherns, D.J. Fermin, Crystal and electronic structure of bismuth thiophosphate, BiPS4: An earth-abundant solar absorber, Chem. Mater. 32 (2020) 1235–1242, https://doi.org/10.1021/acs.chemmater.9b04626.
[37] D. Kang, Y. Park, J.C. Hill, K.S. Choi, Preparation of Bi-based ternary oxide photoanodes BiVO4, Bi2WO6, and Bi2Mo3O12 using dendritic Bi metal electrodes, The Journal of Physical Chemistry Letters 5 (2014) 2994–2999, https://doi.org/10.1021/jz501544k.
[38] K.H. Ye, Z. Chai, J. Gu, X. Yu, C. Zhao, Y. Zhang, W. Mai, BiOI–BiVO4 photoanodes with significantly improved solar water splitting capability: p–n junction to expand solar adsorption range and facilitate charge carrier dynamics, Nano Energy 18 (2015) 222–231, https://doi.org/10.1016/j.nanoen.2015.10.018.
[39] X. Lin, D. Xu, J. Zheng, M. Song, G. Che, Y. Wang, L. Chang, Graphitic carbon nitride quantum dots loaded on leaf-like InVO4/BiVO4 nanoheterostructures with enhanced visible-light photocatalytic activity, J. Alloy. Compd. 688 (2016) 891–898, https://doi.org/10.1016/j.jallcom.2016.07.275.
[40] M. Salavati-Niasari, D. Ghanbari, F. Davar, Synthesis of different morphologies of bismuth sulfide nanostructures via hydrothermal process in the presence of thioglycolic acid, J. Alloy. Compd. 488 (2009) 442–447, https://doi.org/10.1016/j.jallcom.2009.08.152.
[41] V. Stavila, K.H. Whitmire, I. Rusakova, Synthesis of Bi2S3 nanostructures from bismuth (III) thiourea and thiosemicarbazide complexes, Chem. Mater. 21 (2009) 5456–5465, https://doi.org/10.1021/cm902229x.
[42] H. Zimmermann, C.D. Carpentier, R. Nitsche, The crystal structure of bismuth thiophosphate BiPS4, Acta Crystallographica Section B: Structural Crystallography and Crystal, Chemistry 31 (1975) 2003–2006, https://doi.org/10.1107/S0567740875006723.
[43] H. Li, Y. Sun, B. Cai, S. Gan, D. Han, L. Niu, T. Wu, Hierarchically Z-scheme photocatalyst of Ag@ AgCl decorated on BiVO4 (0 4 0) with enhancing photoelectrochemical and photocatalytic performance, Appl Catal B 170 (2015) 206–214, https://doi.org/10.1016/j.apcatb.2015.01.043.
[44] W. Yao, H. Iwai, J. Ye, Effects of molybdenum substitution on the photocatalytic behavior of BiVO4, Dalton Trans. (2008) 1426–1430, https://doi.org/10.1039/B713338C.
[45] L. Zhang, C.Y. Lin, V.K. Valev, E. Reisner, U. Steiner, J.J. Baumberg, Plasmonic enhancement in BiVO4 photonic crystals for efficient water splitting, Small 10 (2014) 3970–3978, https://doi.org/10.1002/smll.201400970.
[46] F.D. Hardcastle, I.E. Wachs, H. Eckert, D.A. Jefferson, Vanadium (V) environments in bismuth vanadates: a structural investigation using Raman spectroscopy and solid state 51V NMR, J. Solid State Chem. 90 (1991) 194–210, https://doi.org/10.1016/0022-4596(91)90135-5.
[47] D.K. Ma, M.L. Guan, S.S. Liu, Y.Q. Zhang, C.W. Zhang, Y.X. He, S.M. Huang, Controlled synthesis of olive-shaped Bi 2 S 3/BiVO 4 microspheres through a limited chemical conversion route and enhanced visible-light-responding photocatalytic activity, Dalton Trans. 41 (2012) 5581–5586, https://doi.org/10.1039/C2DT30099K.
[48] M. Long, W. Cai, J. Cai, B. Zhou, X. Chai, Y. Wu, Efficient photocatalytic degradation of phenol over Co3O4/BiVO4 composite under visible light irradiation, J. Phys. Chem. B 110 (2006) 20211–20216, https://doi.org/10.1021/jp063441z.
[49] W. Luo, Z. Yang, Z. Li, J. Zhang, J. Liu, Z. Zhao, Z. Zou, Solar hydrogen generation from seawater with a modified BiVO4 photoanode, Energ. Environ. Sci. 4 (2011) 4046–4051, https://doi.org/10.1039/C1EE01812D.
[50] J. Yu, A. Kudo, Effects of structural variation on the photocatalytic performance of hydrothermally synthesized BiVO4, Adv. Funct. Mater. 16 (2006) 2163–2169, https://doi.org/10.1002/adfm.200500799.
[51] X. Gao, G. Huang, H. Gao, C. Pan, H. Wang, J. Yan, J. Gao, Facile fabrication of Bi2S3/SnS2 heterojunction photocatalysts with efficient photocatalytic activity under visible light, J. Alloy. Compd. 674 (2016) 98–108, https://doi.org/10.1016/j.jallcom.2016.03.031.
[52] W. Wang, X. Wang, C. Zhou, B. Du, J. Cai, G. Feng, R. Zhang, Bi2S3-nanowire-sensitized BiVO4 sheets for enhanced visible-light photoelectrochemical activities, J. Phys. Chem. C 121 (2017) 19104–19111, https://doi.org/10.1021/acs.jpcc.7b06838.
[53] D. Zhao, W. Wang, W. Zong, S. Xiong, Q. Zhang, F. Ji, X. Xu, Synthesis of Bi2S3/BiVO4 heterojunction with a one-step hydrothermal method based on pH control and the evaluation of visible-light photocatalytic performance, Materials 10 (2017) 891, https://doi.org/10.3390/ma10080891.
[54] Y. Park, K.J. McDonald, K.S. Choi, Progress in bismuth vanadate photoanodes for use in solar water oxidation, Chem. Soc. Rev. 42 (2013) 2321–2337, https://doi.org/10.1039/C2CS35260E.
[55] K. Fan, H. Chen, Y. Ji, H. Huang, P.M. Claesson, Q. Daniel, L. Sun, Nickel–vanadium monolayer double hydroxide for efficient electrochemical water oxidation, Nat. Commun. 7 (2016) 1–9, https://doi.org/10.1038/ncomms11981.
[56] C. Li, X. Zhu, H. Zhang, Z. Zhu, B. Liu, C. Cheng, 3D ZnO/Au/CdS sandwich structured inverse opal as photoelectrochemical anode with improved performance, Adv. Mater. Interfaces 2 (2015) 1500428, https://doi.org/10.1002/admi.201500428.
[57] S. Kumar, S. Ahirwar, A.K. Satpati, Insight into the PEC and interfacial charge transfer kinetics at the Mo doped BiVO4 photoanodes, RSC Adv. 9 (2019) 41368–41382, https://doi.org/10.1039/C9RA08743E.
[58] X. Xiong, L. Fan, G. Chen, Y. Wang, C. Wu, D. Chen, S. Ren, Boosting water oxidation performance of CuWO4 photoanode by surface modification of nickel phosphate, Electrochim. Acta 328 (2019), https://doi.org/10.1016/j.electacta.2019.135125.
[59] N. Li, X. Wu, M. Wang, K. Huang, J. He, W. Ma, S. Feng, Facile preparation of BiVO4/FeVO4 heterostructure for efficient water-splitting applications, Int. J. Hydrogen Energy 44 (2019) 23046–23053, https://doi.org/10.1016/j.ijhydene.2019.07.063.
[60] G. Fang, G., Liu, Z., Han, C., Wang, P., Ma, X., Lv, H., & Tong, Z., Promising CoFe-NiOOH Ternary Polymetallic Cocatalyst for BiVO4-Based Photoanodes in Photoelectrochemical Water Splitting, ACS Applied Energy Materials 4 (2021) 3842–3850, https://doi.org/10.1021/acsaem.1c00247.
[61] X. Han, Y. Wei, J. Su, Y. Zhao, Low-cost oriented hierarchical growth of BiVO4/rGO/NiFe nanoarrays photoanode for photoelectrochemical water splitting, ACS Sustain. Chem. Eng. 6 (2018) 14695–14703, https://doi.org/10.1021/acssuschemeng.8b03259.
[62] Y. Zhu, J. Ren, X. Yang, G. Chang, Y. Bu, G. Wei, D. Yang, Interface engineering of 3D BiVO 4/Fe-based layered double hydroxide core/shell nanostructures for boosting photoelectrochemical water oxidation, J. Mater. Chem. A 5 (2017) 9952–9959, https://doi.org/10.1039/C7TA02179H.
[63] Y. Wei, J. Su, X. Wan, L. Guo, L. Vayssieres, Spontaneous photoelectric field-enhancement effect prompts the low cost hierarchical growth of highly ordered heteronanostructures for solar water splitting, Nano Res. 9 (2016) 1561–1569, https://doi.org/10.1007/s12274-016-1050-9.
[64] F.S. Hegner, I. Herraiz-Cardona, D. Cardenas-Morcoso, N. López, J.R. Galán-Mascarós, S. Gimenez, Cobalt hexacyanoferrate on BiVO4 photoanodes for robust water splitting, ACS Appl. Mater. Interfaces 9 (2017) 37671–37681, https://doi.org/10.1021/acsami.7b09449.
[65] M.A. Mahadik, H.S. Chung, S.Y. Lee, M. Cho, J.S. Jang, In-situ noble fabrication of Bi2S3/BiVO4 hybrid nanostructure through a photoelectrochemical transformation process for solar hydrogen production, ACS Sustain. Chem. Eng. 6 (2018) 12489–12501, https://doi.org/10.1021/acssuschemeng.8b03140.
[66] M. Wang, Q. Wang, P. Guo, Z. & Jiao,, In situ fabrication of nanoporous BiVO4/Bi2S3 nanosheets for enhanced photoelectrochemical water splitting, J. Colloid Interface Sci. 534 (2019) 338–342, https://doi.org/10.1016/j.jcis.2018.09.056.1.
[67] M. Huang, J. Bian, W. Xiong, C. Huang, R. Zhang, Low-dimensional Mo: BiVO 4 photoanodes for enhanced photoelectrochemical activity, J. Mater. Chem. A 6 (2018) 3602–3609, https://doi.org/10.1039/C7TA11132K.
[68] R.T. Gao, D. He, L. Wu, K. Hu, X. Liu, Y. Su, L. Wang, Towards Long-Term Photostability of Nickel Hydroxide/BiVO4 Photoanodes for Oxygen Evolution Catalysts via In Situ Catalyst Tuning, Angew. Chem. 132 (2020) 6272–6277, https://doi.org/10.1002/ange.201915671.
[69] R.T. Gao, L. Wang, Stable Cocatalyst-Free BiVO4 Photoanodes with Passivated Surface States for Photocorrosion Inhibition, Angew. Chem. Int. Ed. 59 (2020) 23094–23099, https://doi.org/10.1002/anie.202010908.
[70] L. Chen, D. Meng, X. Wu, A. Wang, J. Wang, Y. Wang, M. Yu, In situ synthesis of V4+and Ce3+self-doped BiVO4/CeO2 heterostructured nanocomposites with high surface areas and enhanced visible-light photocatalytic activity, J. Phys. Chem. C 120 (2016) 18548–18559, https://doi.org/10.1021/acs.jpcc.6b04131.
[71] L. Chen, S.F. Yin, S.L. Luo, R. Huang, Q. Zhang, T. Hong, P.C.T. Au, Bi2O2CO3/BiOI photocatalysts with heterojunctions highly efficient for visible-light treatment of dyecontaining wastewater, Ind. Eng. Chem. Res. 51 (2012) 6760–6768, https://doi.org/10.1021/ie300567y.
[72] L. Zou, H. Wang, X. Wang, High efficient photodegradation and photocatalytic hydrogen production of CdS/BiVO4 heterostructure through Z–scheme process, ACS. Sustain, Chem. Eng. 5 (2017) 303–309, https://doi.org/10.1021/acssuschemeng.6b01628.
[73] J. Wang, J. Jin, X. Wang, S. Yang, Y. Zhao, Y. Wu, J. Sun, Facile fabrication of novel BiVO4/Bi2S3/MoS2 np heterojunction with enhanced photocatalytic activities towards pollutant degradation under natural sunlight, J. Colloid Interface Sci. 505 (2017) 805–815, https://doi.org/10.1016/j.jcis.2017.06.085.
[74] X. Gao, Z. Wang, F. Fu, X. Li, W. Li, 2D double-layer-tube-shaped structure Bi2S3/ZnS heterojunction with enhanced photocatalytic activities, Phys. B 474 (2015) 81–89, https://doi.org/10.1016/j.physb.2015.06.002.